

Printing mesoscale architectures

Jordan R. Raney and Jennifer A. Lewis

The ability to pattern materials in three dimensions is crucial for structural, optical, electronic, and energy applications. Three-dimensional printing allows one to design and rapidly fabricate materials in complex shapes without the need for expensive tooling, dies, or lithographic masks. A growing palette of printable materials, coupled with the ability to programmably control mesoscale architecture, open new avenues for creating designer materials with unprecedented performance.

Introduction

New methods for patterning materials at the mesoscale, which lies between the molecular and macroscopic lengths scales, are driving scientific and technological advances in multiple areas, including lightweight structures, antennas, batteries, displays, and photonics. The broad diversity of potentially relevant materials, length scales, and architectures underscores the need for flexible patterning approaches. The term “three-dimensional (3D) printing” describes additive manufacturing methods that employ a computer-controlled translation stage, which moves a pattern-generating device in the form of ink deposition nozzle(s) or laser-writing optics, to fabricate materials layer by layer.^{1–14} Since the 1980s, several ink- and light-based techniques have been introduced to pattern materials in three dimensions (**Figure 1**).

Ink-based printing approaches consist of filamentary and droplet-based methods. Printable inks are typically formulated from particulate and polymeric species that are suspended or dissolved in a liquid or heated to achieve the desired rheological (or flow) behavior. Specific parameters of interest include the ink viscosity, surface tension, shear yield stress, and viscoelastic properties (i.e., the shear elastic and loss moduli) which must be tailored for each printing method. In droplet-based methods, materials are deposited using printheads similar to those employed in desktop document printing. Several 3D printing methods rely on this basic approach, including inkjet printing on a powder bed,¹⁵ direct inkjet printing,^{16–18} and hot-melt printing.¹⁹

The “inks” are composed of low-viscosity fluids that must be removed by evaporation, ultraviolet- (UV-) curable resins that are polymerized upon printing, or wax-based inks that are heated during droplet formation and then solidified upon impact. The fluid dynamics involved in droplet formation, wetting, and spreading play an important, yet also limiting, role in defining the surface roughness and minimum feature size of materials patterned by inkjet printing methods. Typical values for the ink viscosity, droplet size, and velocity are 2–20 mPa·s, 10–30 μm, and 1–10 m/s, respectively, making it inherently difficult to jet concentrated suspensions or polymer solutions without clogging.

Unlike droplet-based methods, filamentary printing methods^{20,21} allow for a broader range of ink designs, feature sizes, and geometries. In this approach, a viscoelastic ink is deposited as a continuous filament in a layer-wise build sequence. In the earliest embodiment, known as fused-deposition modeling,^{22,23} thermoplastic filaments are fed through a hot extrusion head, printed, and solidified as they cool below their glass-transition temperature. Recently, direct-writing of viscoelastic inks under ambient conditions has emerged as a viable alternative. Several concentrated colloidal,²⁴ nanoparticle,²⁵ fugitive organic (used to sacrificially pattern empty channels in a matrix material),²⁶ and polyelectrolyte³ inks have been developed for printing complex 3D architectures. Continuous solids,²⁷ high-aspect-ratio walls,^{28,29} or spanning features^{2,7,24} can be constructed. Typical values for the ink viscosity, filament

Jordan R. Raney, Harvard University, USA; raney@seas.harvard.edu
Jennifer A. Lewis, Harvard University, USA; jalewis@seas.harvard.edu
DOI: 10.1557/mrs.2015.235

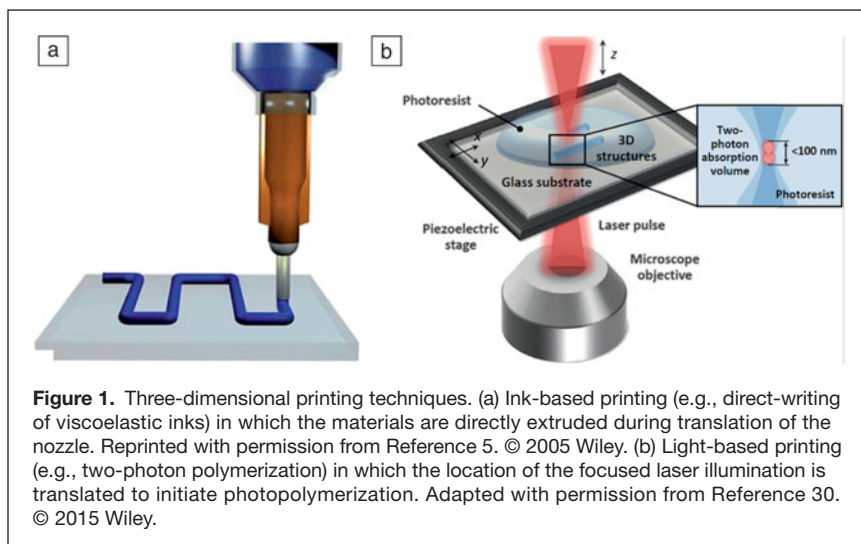


Figure 1. Three-dimensional printing techniques. (a) Ink-based printing (e.g., direct-writing of viscoelastic inks) in which the materials are directly extruded during translation of the nozzle. Reprinted with permission from Reference 5. © 2005 Wiley. (b) Light-based printing (e.g., two-photon polymerization) in which the location of the focused laser illumination is translated to initiate photopolymerization. Adapted with permission from Reference 30. © 2015 Wiley.

diameter, and printing speed are 10^2 – 10^6 mPa·s (depending on the shear rate), 1 μm to 1 mm, and 1 mm/s to 10 cm/s, respectively.

Light-based printing methods create patterned materials via two-photon polymerization^{10,30,31} (Figure 1b), UV curing,^{1,32–35} selective laser melting,³⁶ or electron-beam (e-beam) welding.^{37,38} Each method places different demands on the patterning tool and the physicochemical properties of the material being patterned. Photopolymerizable resins are used in stereolithography and digital projection lithography, whereas polymer and metal powders are fused together by selective laser and e-beam melting. While UV, nanosecond pulsed, excimer, and Nd:YAG (Nd-doped yttrium aluminum garnet) lasers are most commonly used, shorter pulse lasers, such as pico- and femtosecond lasers, and electron beams are also finding applications as precision patterning tools. These printing methods are capable of generating complex 3D structures with self-supporting features at resolutions comparable to (or better than) those achieved by ink-based printing techniques. An example of this would be two-photon lithography, where a photoresist that is transparent to the laser beam is selected, with the photon energy below the absorption band of the material. For a small, controlled focal volume, sufficient intensity exists to produce multiphoton absorption events, which can meet the energy threshold necessary to achieve photopolymerization.¹⁰ Recent advances have enabled remarkable resolution (~ 100 nm) using this approach,^{30,31} although writing speeds and build heights are limited.³⁹

In this article, we highlight several mesoscale architectures that are uniquely enabled by 3D printing. The mesoscale is of specific interest, because it can be readily tailored by these programmable assembly methods. As a first demonstration, we introduce architected cellular materials for structural, photonic, and other applications. Next, we describe new electronic devices composed of spanning and conformal conductive features. Finally, multimaterial 3D printing of rechargeable microbatteries and light-emitting diodes (LEDs) is discussed.

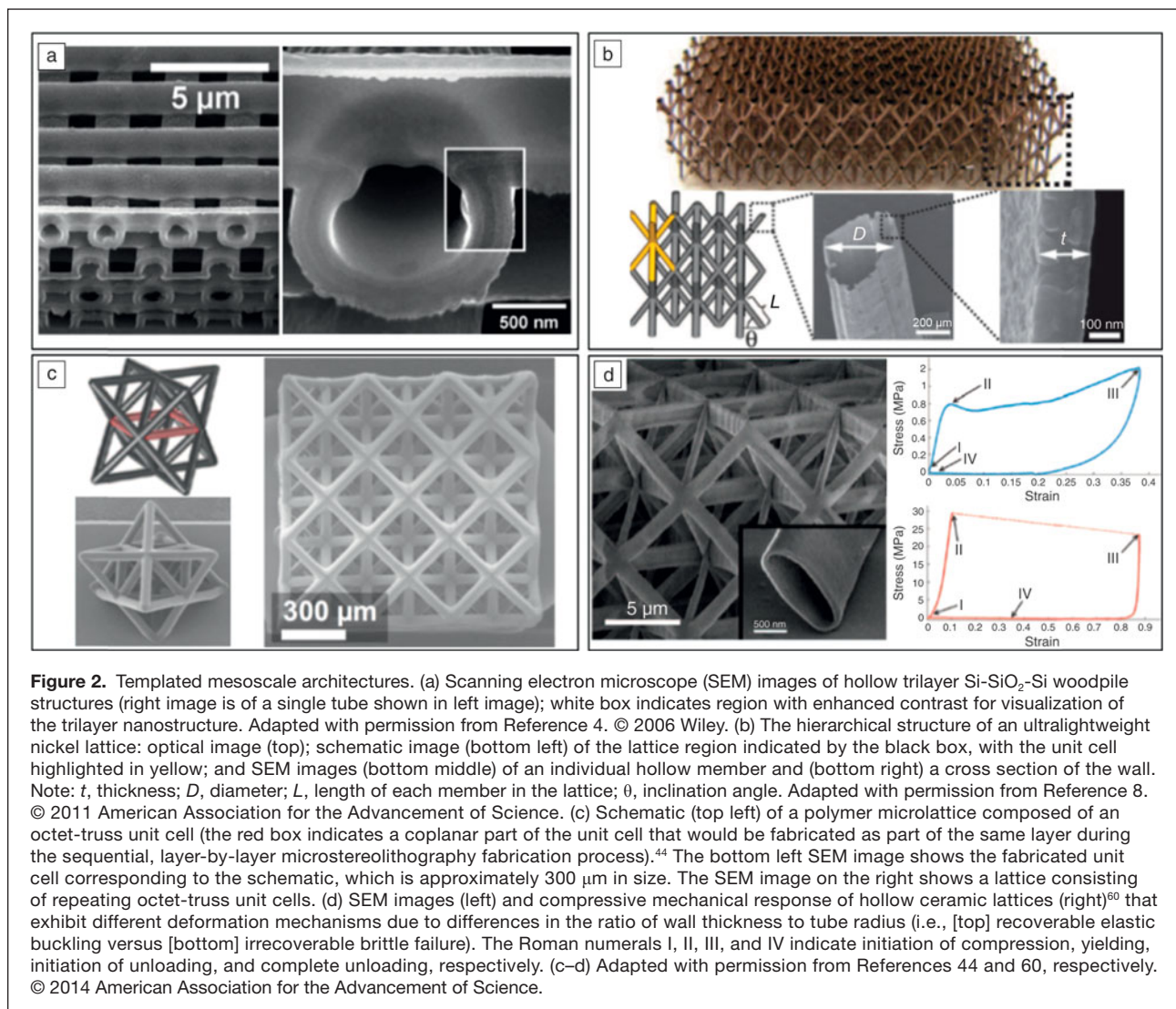
Lightweight architectures

The ability to rapidly fabricate 3D mesoscale architectures with optimized topology and composition would enable myriad applications, including photonics,^{40–43} structural materials,^{8,44,45} catalyst supports,^{46,47} filtration media,^{48,49} and heat exchangers.⁵⁰ Nature is replete with examples of complex 3D architectures, such as butterfly wings,⁵¹ wood,⁵² bone,⁵³ beaks,⁵⁴ and the dactyl club (an appendage with a claw at the terminal end) that certain shrimp possess⁵⁵ to name a few, with hierarchical features seamlessly integrated across many length scales. Their remarkable properties, structural color⁵¹ or high specific stiffness and strength, arise in part from mesoscopic features,⁵⁶ including compositional periodicity,⁵¹ gradients,⁵⁴ fiber alignment,⁵⁷ and other forms of hierarchical complexity.⁵³ Together, these attributes have important implications for the macroscopic response and the scaling laws associated with each structure.⁴⁴

Inspired by nature, researchers have focused on creating synthetic analogues via self- and directed-assembly methods. Specifically, programmable methods, such as 3D printing, are being increasingly used to create architected materials, opening up an entirely new design space.^{8,29,39,44,45,58–62} Simple structures fabricated from a single material can exhibit enhanced or even fundamentally new properties. At a fixed material and bulk density, the careful design of architecture can enable control over light propagation or the mode of mesoscopic deformation (e.g., bending versus stretching of mesoscopic beams). 3D printed architectures can also serve as templates for patterning materials.

Polymer architectures created by ink- and light-based 3D printing approaches can be transformed into semiconducting,⁴ metallic,⁸ and ceramic⁶⁰ structures that are difficult to directly print at these length scales.⁴⁴ One elegant strategy is to conformally coat printed polymer architectures via gas-phase or solution-based techniques, such as chemical vapor deposition (CVD),⁴ atomic layer deposition,⁶⁰ or electroless plating.⁸ This strategy allows structural control over features at finer resolution than those achieved by the printing method used (Figure 2). For instance, hollow semiconducting, metallic, and ceramic lattices with ultrathin walls have been produced by conformal coating followed by etching away the underlying polymeric features. Both optical and mechanical properties can be dramatically tailored by this combined approach.

A seminal example is shown in Figure 2a, in which printed polymer lattices are transformed into hollow woodpile architectures composed of silicon for photonic applications. Silicon is an ideal material for photonic crystals, because it has a high refractive index ($n \sim 3.45$). The woodpile structure is particularly well-suited for microfabrication⁴² and direct-write assembly⁴ methods. To fabricate these architectures, concentrated polyelectrolyte inks are printed as face-centered-tetragonal



lattices.^{3,4} These structures are then coated with silica using a room-temperature CVD process, followed by polymer removal by etching. Finally, the hollow silica features are coated with silicon using a high-temperature CVD process. The final architecture, which is composed of an interconnected array of cylinders with a total wall thickness of ~ 300 nm,⁴ exhibits a partial photonic bandgap.

Ultralight architected metals with densities on the order of 1 mg cm^{-3} have been recently fabricated by combining a light-based patterning method with conformal coating.^{8,44} Their wall thickness gives rise to an additional relevant length scale, which can introduce dramatic new mechanical effects, observable at the macroscale during mechanical loading and unloading. Electroless nickel plating is one approach that has been used to conformally coat polymer scaffolds with a thickness of approximately 100 nm.⁸ The hollow nickel-phosphorus structure left behind after the polymer is etched away exhibits unexpected elastic recovery from compressive strains, a result of the introduction of new modes of local

deformation (e.g., elastic shell buckling) and associated stable relief cracks at the nodes.

Scaling relationships, determined previously for porous materials,⁶³ relate their macroscopic properties to their relative density, ρ/ρ_s . The relative density is defined as the total bulk density of the porous structure, including void space (ρ), divided by the density of the solid material from which the structure is assembled (ρ_s). It is often desirable in engineering applications to use cellular solids that are as low-density as possible for a given function. Lower-density structures can be constructed by simply using lower relative densities, but desired properties often decrease by larger factors. For example, the relative stiffness of a typical stochastic foam scales as $(E/E_s) \propto (\rho/\rho_s)^2$, where E is Young's modulus of the bulk structure and E_s is Young's modulus of the solid material that the structure is made from.⁶³ If an ordered cellular structure is designed to deform predominantly via bending, it exhibits a comparable scaling relationship.⁴⁴ However, different motifs can force deformation to occur via stretching, rather than

bending, of the members, as an example. This results in a linear scaling relationship between relative stiffness and relative density, or $(E/E_s) \propto (\rho/\rho_s)$. Thus, at its simplest, the ability to tune a structure can enable control of the deformation mechanism. This can determine the relevant scaling behavior, which also affects the failure modes of the system.

Recently, sufficiently long and thin hollow ceramic tubes with wall thicknesses less than 20 nm have been observed to locally deform via reversible elastic shell buckling, enabling these architectures to fully recover after compression of up to 50% strains (Figure 2d, top plot), in sharp contrast to the brittle response expected for ceramics (which is observed when the geometry is slightly changed—Figure 2d, bottom plot).⁶⁰ While related size effects at the nanoscale, such as size-dependent mechanical properties, have been reported previously,^{64,65} 3D printing opens new avenues for achieving these benefits in larger engineering structures.

Beyond control over the deformation mechanism, architected materials can also be designed and fabricated to exhibit more exotic responses, such as negative stiffness⁶¹ or negative Poisson's ratio.³⁹ By controlling the arrangement of simple cylindrical features of submillimeter diameter in a “woodpile” structure via direct-write 3D printing, macroscopic structures can be produced that exhibit negative shear stiffness under certain conditions.⁶¹ Each layer consists of a number of parallel cylinders that are oriented orthogonal to those in the previous layer. In a simple cubic structure, every other layer is printed in the same position, whereas they are laterally offset by a half-period in a face-centered-tetragonal geometry. If the cylinders are arranged in a simple cubic structure, then the structures, when confined by a static force in one direction, tend to snap between different configurations as a shear stress is applied in a direction orthogonal to the static stress. Upon changing their arrangement from a simple cubic to a face-centered-tetragonal structure, a more conventional shear stiffness response is obtained.

Another macroscopic property that can be engineered through mesoscopic architecture is the Poisson ratio, $\nu = -\varepsilon_t/\varepsilon_l$; this ratio relates the extent to which a material deforms laterally (transverse strain, ε_t) when a defined deformation is applied in a direction perpendicular to this (longitudinal strain, ε_l). Typically, when materials are pulled in tension along one axis, they contract in the orthogonal directions, giving rise to a positive Poisson's ratio. However, mesoscopic architectures have been designed that produce a negative Poisson's

ratio at the macroscale, where tension along one axis leads to expansion along the orthogonal axes.^{66,67} These auxetic materials have been fabricated by direct-laser writing with submicron features.³⁹ Only through 3D printing has the fabrication of nonstochastic negative Poisson's ratio structures, previously assembled by hand,⁶⁷ reached sufficient resolution and throughput to be considered for practical use (e.g., as damping materials or indentation-resistant structural materials).

3D printing of composite architectures has also been recently demonstrated.^{45,68–72} In one approach, direct-writing with fiber-reinforced epoxy inks has been reported (Figure 3).⁴⁵ During printing, the ink experiences a high shear environment within the nozzle that induces alignment of anisotropic fillers along the print path (Figure 3a). Macroscopic cellular architectures, such as the honeycomb structure shown in Figure 3b, can be rapidly fabricated with different print paths to yield different spatial distributions

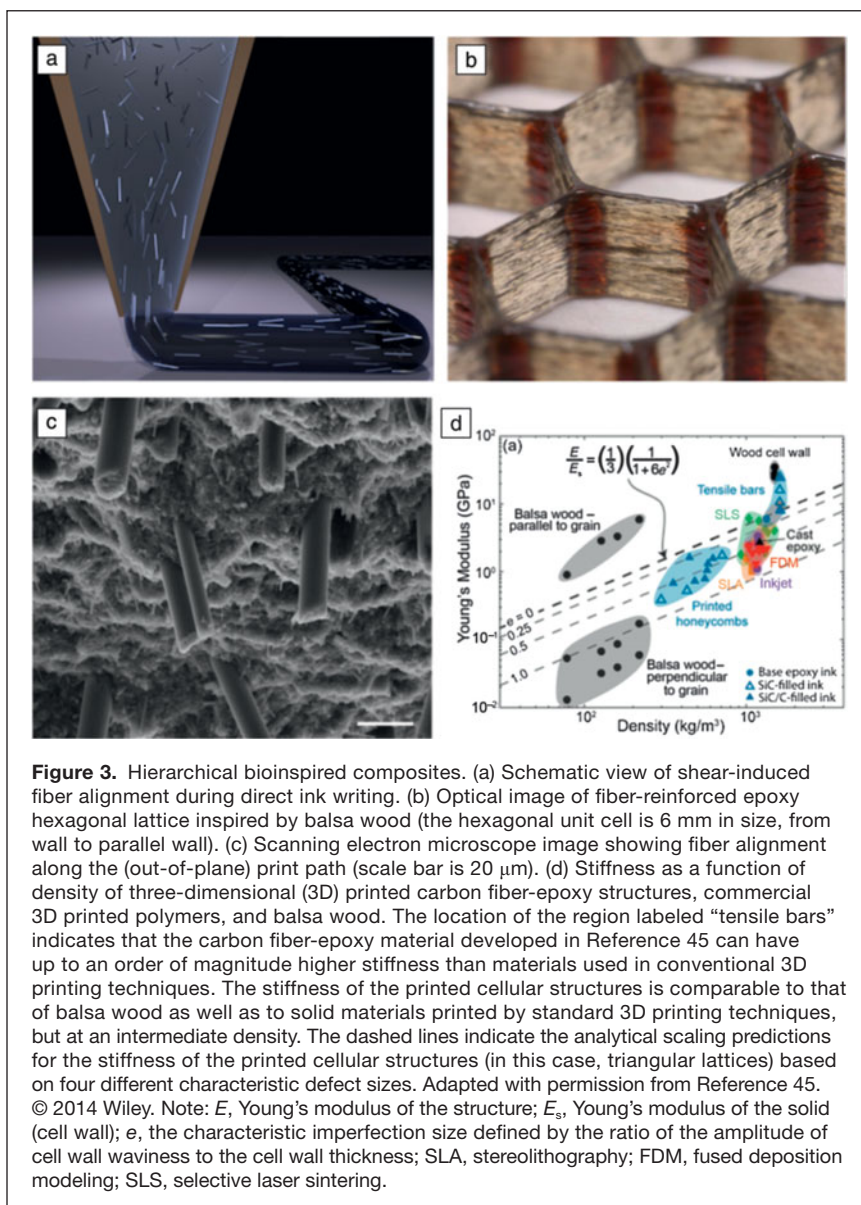


Figure 3. Hierarchical bioinspired composites. (a) Schematic view of shear-induced fiber alignment during direct ink writing. (b) Optical image of fiber-reinforced epoxy hexagonal lattice inspired by balsa wood (the hexagonal unit cell is 6 mm in size, from wall to parallel wall). (c) Scanning electron microscope image showing fiber alignment along the (out-of-plane) print path (scale bar is 20 μ m). (d) Stiffness as a function of density of three-dimensional (3D) printed carbon fiber-epoxy structures, commercial 3D printed polymers, and balsa wood. The location of the region labeled “tensile bars” indicates that the carbon fiber-epoxy material developed in Reference 45 can have up to an order of magnitude higher stiffness than materials used in conventional 3D printing techniques. The stiffness of the printed cellular structures is comparable to that of balsa wood as well as to solid materials printed by standard 3D printing techniques, but at an intermediate density. The dashed lines indicate the analytical scaling predictions for the stiffness of the printed cellular structures (in this case, triangular lattices) based on four different characteristic defect sizes. Adapted with permission from Reference 45. © 2014 Wiley. Note: E , Young's modulus of the structure; E_s , Young's modulus of the solid (cell wall); e , the characteristic imperfection size defined by the ratio of the amplitude of cell wall waviness to the cell wall thickness; SLA, stereolithography; FDM, fused deposition modeling; SLS, selective laser sintering.

of fiber orientation. The uniform local alignment of the fibers (Figure 3c) results in anisotropic mechanical properties (Figure 3d), akin to those observed in natural materials, such as balsa wood.⁵² Alternate approaches combine stiff and soft elements with disparate mechanical properties to engineer lightweight materials with excellent toughness, impact resistance, and specific mechanical properties.^{68–71} For example, nacre-like architectures⁷³ of alternating stiff and soft polymer features have been printed.⁶⁹ These mesoscale architectures mimic that of nacre, which exhibits mechanical properties that are superior to those of the individual soft and stiff constituents, a result of crack diversion, breaking of mineral bridges, topological interlocking of the stiff components, and viscoelastic behavior of the soft phase during deformation.⁵⁶ The possibilities for designing and fabricating architected materials with unprecedented performance are nearly endless.

3D electronics

The ability to rapidly fabricate 3D electronics would enable many applications, including displays, solid-state lighting, microbatteries, sensors, and wearable and biomedical devices with embedded circuitry in arbitrary form factors. High-resolution, planar patterning of functional materials has been possible for some time. Roll-to-roll⁷⁴ and inkjet printing⁷⁵ have been used to create functional features such as polymeric transistors over large areas, and “dip-pen” nanolithography⁷⁶ (which uses the tip of an atomic force microscope to place collections of molecules in ordered patterns on a substrate via capillary transport) has been used to create functional features with nanoscale precision. However, it is far more challenging to design functional materials that can be patterned in three dimensions.

One enabling advancement is the ability to print electrically conductive features in flexible, stretchable, spanning, and conformal motifs (Figure 4a–d).⁷⁷ These features can serve as interconnects for photovoltaic microcells and LED arrays or as the conductive features necessary to produce functional antennae (Figure 4e–f). With the use of direct-writing, concentrated silver inks (>70 wt% Ag) have been patterned at room temperature at resolutions approaching 1 μm (Figure 4a–d).⁷ Their viscoelastic properties allow the ink to be printed out of plane and across gaps (Figure 4a) to form self-supporting features, such as bridges, that connect functional devices (Figure 4b–d). Upon thermal annealing at 150–550°C, the electrical resistivity of the printed silver interconnects dramatically reduces. These inks have also been patterned conformally on both concave

and convex glass hemispheres to produce customized, 3D electrically small antennas.⁷⁷ An antenna is electrically small when its electrical size, defined as the product of the wavenumber k and the radius a of the smallest possible sphere that can encompass the entire antenna, is less than 0.5. Efficient hemispherical design (Figure 4e) requires patterning of conductive features on curvilinear surfaces. Figure 4f highlights the antenna performance, which is given by the voltage standing wave ratio (VSWR) as a function of frequency, an indicator of how well energy is coupled from source to antenna. A lower VSWR indicates a stronger coupling between the wave and the antenna (a VSWR value of 1 corresponds to perfect coupling), and the width defines the impedance bandwidth. The antenna efficiency is greater than 70%, at a bandwidth that matches the value predicted by computer simulation.

Meniscus-confined electrodeposition is another approach for directly writing conductive features.⁷⁸ For example, a precursor

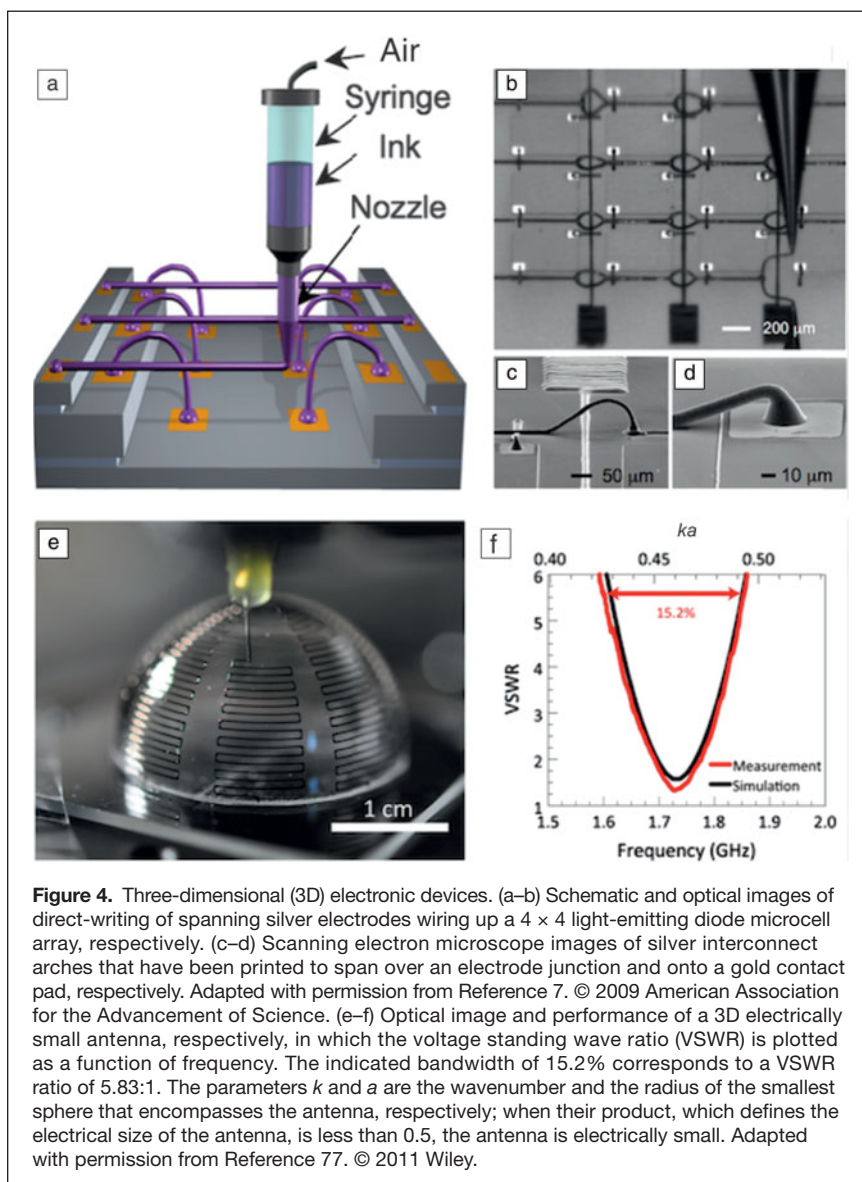


Figure 4. Three-dimensional (3D) electronic devices. (a–b) Schematic and optical images of direct-writing of spanning silver electrodes wiring up a 4×4 light-emitting diode microcell array, respectively. (c–d) Scanning electron microscope images of silver interconnect arches that have been printed to span over an electrode junction and onto a gold contact pad, respectively. Adapted with permission from Reference 7. © 2009 American Association for the Advancement of Science. (e–f) Optical image and performance of a 3D electrically small antenna, respectively, in which the voltage standing wave ratio (VSWR) is plotted as a function of frequency. The indicated bandwidth of 15.2% corresponds to a VSWR ratio of 5.83:1. The parameters k and a are the wavenumber and the radius of the smallest sphere that encompasses the antenna, respectively; when their product, which defines the electrical size of the antenna, is less than 0.5, the antenna is electrically small. Adapted with permission from Reference 77. © 2011 Wiley.

electrolyte solution, such as CuSO_4 , is brought near a conductive substrate in a micropipette, allowing the meniscus to make contact. Upon applying a small voltage, copper metal is electrodeposited from the precursor solution, or “ink,” onto the substrate. Arbitrary conductive features can be patterned by translating the micropipette in a prescribed manner. While this approach obviates the need for post-processing, it is limited by slow writing speeds (about 250 nm s^{-1} for Cu wires of approximately $1 \mu\text{m}$ in diameter) and the need to maintain continuous electrical contact with a conductive substrate during printing.

Recently, direct-writing of metals that are liquid at room temperature, specifically, eutectic gallium and indium (EGaIn), has been pursued to create interconnects for flexible, stretchable electronics.^{79–82} Immediately upon printing, an ultrathin, passivating oxide layer forms on the outer surface of the liquid metal when exposed to air. This imparts sufficient mechanical stability to allow this low-viscosity liquid to retain its shape without wetting and spreading, resulting in freestanding 3D shapes with a resolution of $10 \mu\text{m}$ or less. However, since these electrodes are inherently a liquid under ambient conditions, the printed features must be fully encapsulated within the functional device of interest.

Multimaterial 3D printing of mesoscale architectures is an emerging area of interest (Figure 5). Recent advances include printing of rechargeable lithium- (Li-) ion microbatteries²⁹ and LED arrays.⁸³ Specifically, 3D microbatteries have been fabricated²⁹ by co-printing $\text{Li}_4\text{Ti}_5\text{O}_{12}$ (LTO) as an anode material and LiFePO_4 (LFP) as a cathode material in interdigitated, high-aspect-ratio motifs. These active materials were chosen because of their minimal volume change during charge/discharge cycles.^{84,85} In both cases, inks were designed with LTO or LFP nanoparticles in solution, with total solid loadings of approximately 60 wt%. These concentrated viscoelastic inks exhibit a strong shear thinning response and readily flow through nozzles as small as $30 \mu\text{m}$ in diameter. The anode and cathode were printed with high fidelity in the form of high-aspect-ratio, interdigitated features (Figure 5a–b). Subsequent heating to 600°C removes the organic processing aids and partially sinters the nanoparticles. The anode and cathode remain porous to ensure superior ion and electron transport during operation.²⁹ Figure 5c shows the areal capacity of the batteries for up to 30 charge/discharge cycles with minimal capacity fade. Their areal energy and power densities are among the highest

reported to date for microbatteries.²⁹ Moreover, rechargeable microbatteries of nearly arbitrary size, geometry, and capacity can be fabricated by this programmable method that are well-matched to the specific needs and physical dimensions of each targeted application.

Multimaterial mesoscale architectures require not only that each material meets specific functional requirements, but also that the printed materials are compatible with one another. These challenges had to be overcome in the recent fabrication

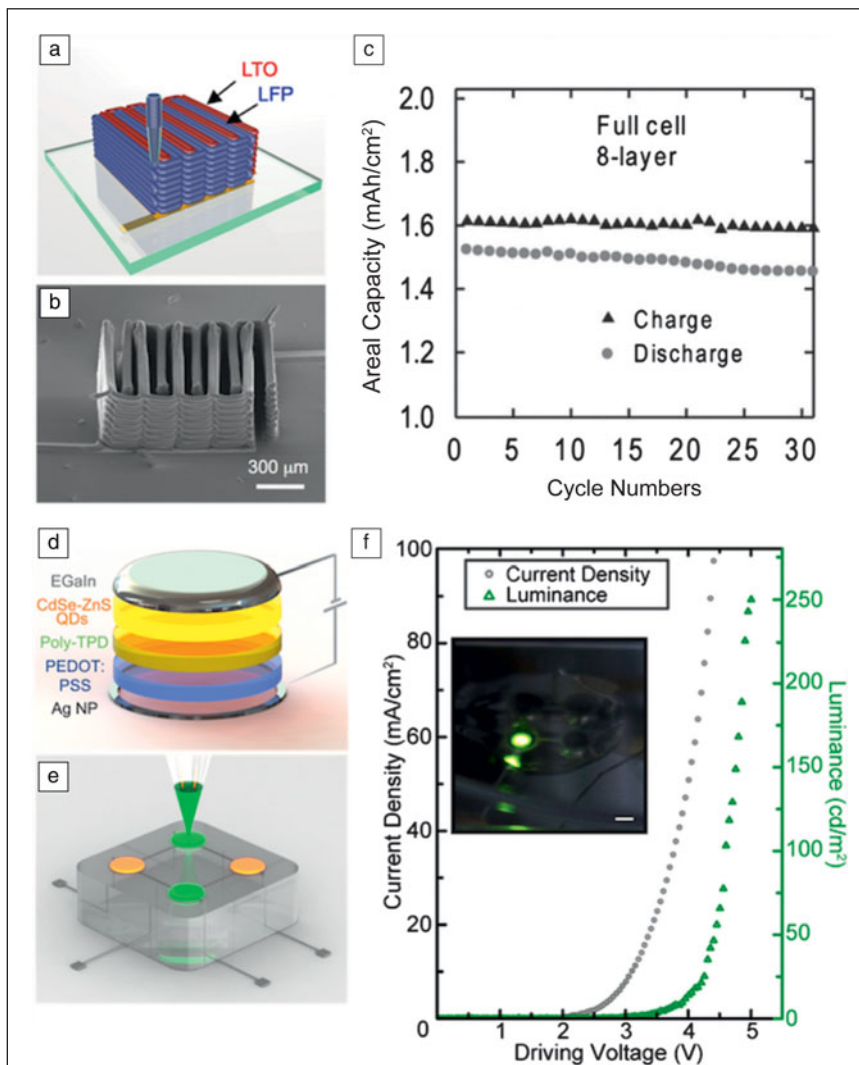


Figure 5. Three-dimensional printed microbatteries and light-emitting diodes (LEDs). (a–b) Schematic view and scanning electron microscope image of printed lithium-ion microbatteries, respectively. (c) Areal capacity of printed microbatteries as a function of charge–discharge cycle showing minimal degradation of performance over the first 30 cycles. (a–c) Adapted with permission from Reference 29. © 2013 Wiley. (d–e) Schematic views of printed quantum dot light-emitting diodes (QD-LEDs), which show an individual LED and an LED array (with the two colors illustrating the tunability of the emission wavelength based on the size of the quantum dots), respectively. (f) Current density–voltage curves and forward luminance output of a printed green QD-LED, demonstrating the functionality of the QD-LEDs fabricated in this highly customizable approach (scale bar of inset optical image is 2 mm). (d–f) Adapted with permission from Reference 83. © 2014 American Chemical Society. Note: LTO, $\text{Li}_4\text{Ti}_5\text{O}_{12}$; LFP, LiFePO_4 ; EGaIn, eutectic gallium indium; TPD, *N,N'*-bis(4-butylphenyl)-*N,N'*-bis(phenyl)-benzidine; PEDOT:PSS, poly(ethylenedioxythiophene) polystyrene sulfonate; NP, nanoparticle.

of 3D printed LEDs (Figure 5d–f).⁸³ Specifically, quantum dot light-emitting diodes (QD-LEDs) were printed, which required the development and co-printing of several different functional inks to produce light emission, charge transport, conductive leads, and UV-curable adhesion layers. The multi-layer architectures necessitated the use of orthogonal solvents that would not “mix” with underlying patterned features. While the brightness of the printed QD-LEDs is more than an order of magnitude lower than the best reported to date via solution-processing, this approach constitutes an impressive demonstration of multimaterial 3D printing of optoelectronic devices at the mesoscale.

The future possibilities of 3D printing as a platform for creating customized, fully integrated devices are vast. Additionally, hybrid strategies can be implemented in which 3D printing is combined with automated pick-and-place methods to create more complicated electronic devices.⁸⁶ The development of new functional inks, flexible printing platforms, and software that integrates computer-aided design with electronic device layout capabilities in three dimensions is essential to transforming how electronic devices are designed and integrated into our daily lives.

Future perspective

3D printing is rapidly advancing beyond patterning complex forms to directly embedding function. Nearly arbitrary, 3D mesoscale architectures can be printed with minimum feature sizes ranging from ~100 nm to 100 μm from multiple classes of materials. By digitally designing and building 3D mesoscale architectures, one can fundamentally control their macroscale properties. While multimaterial integration is still in its infancy, one can envision a “model to make” strategy that begins with multiscale modeling, coupled with computer-aided design, which is then transformed into complex physical embodiments through the synthesis and patterning of functional, structural, and even biological inks, to yield 3D architectures with as yet unimagined performance.

Acknowledgment

We gratefully acknowledge support from DOE EFRC on Light-Material Interactions in Energy Conversion (Award Number: DE-SC0001293) funded by the US Department of Energy, Office of Science, Basic Energy Sciences.

References

1. X. Zhang, X.N. Jiang, C. Sun, *Sens. Actuators A Phys.* **77**, 149 (1999).
2. J.E. Smay, J. Cesarano III, J.A. Lewis, *Langmuir* **18**, 5429 (2002).
3. G.M. Gratson, M. Xu, J.A. Lewis, *Nature* **428**, 386 (2004).
4. G.M. Gratson, F. Garcia-Santamaria, V. Lousse, M. Xu, S. Fan, J.A. Lewis, P.V. Braun, *Adv. Mater.* **18**, 461 (2006).
5. D. Therriault, R.F. Shepherd, S.R. White, J.A. Lewis, *Adv. Mater.* **17**, 395 (2005).
6. J.A. Lewis, *Adv. Funct. Mater.* **16**, 2193 (2006).
7. B.Y. Ahn, E.B. Duoss, M.J. Motala, X. Guo, S.-I. Park, Y. Xiong, J. Yoon, R.G. Nuzzo, J.A. Rogers, J.A. Lewis, *Science* **323**, 1590 (2009).
8. T.A. Schaedler, A.J. Jacobsen, A. Torrents, A.E. Sorensen, J. Lian, J.R. Greer, L. Valdivia, W.B. Carter, *Science* **334**, 962 (2011).
9. T. Billiet, M. Vandenhaute, J. Schelfhout, S. van Vlierbergh, P. Dubruel, *Biomaterials* **33**, 6020 (2012).
10. M. Rohrig, M. Thiel, M. Worgull, H. Holscher, *Small* **8**, 3009 (2012).
11. O. Ivanova, C. Williams, T. Campbell, *Rapid Prototyp. J.* **19**, 353 (2013).
12. D. Jang, L.R. Meza, F. Greer, J.R. Greer, *Nat. Mater.* **12**, 893 (2013).
13. W.E. Frazier, *J. Mater. Eng. Perform.* **23**, 1917 (2014).
14. R.D. Farahani, K. Chizari, D. Therriault, *Nanoscale* **6**, 10470 (2014).
15. E. Sachs, M. Cima, P. Williams, D. Brancazio, J. Cornie, *J. Eng. Ind. Trans. ASME* **114**, 481 (1992).
16. J.H. Song, M.J. Edirisinghe, J.R.G. Evans, *J. Am. Ceram. Soc.* **82**, 3374 (1999).
17. M. Mott, J.R.G. Evans, *Mater. Sci. Eng. A* **271**, 344 (1999).
18. B.Y. Tay, M.J. Edirisinghe, *J. Mater. Res.* **16**, 373 (2001).
19. K.A.M. Seerden, N. Reis, J.R.G. Evans, P.S. Grant, J.W. Halloran, B. Derby, *J. Am. Ceram. Soc.* **84**, 2514 (2001).
20. J. Cesarano III, P. Calvert, “Freeforming Objects with Low-Binder Slurry,” US Patent 6,027,326 (2000).
21. J. Cesarano III, R. Segalman, P. Calvert, *Ceram. Ind.* **148**, 94 (1998).
22. S.S. Crump, “Apparatus and Method for Creating Three-Dimensional Objects,” US Patent 5,121,329 A (1992).
23. S.S. Crump, “Modeling Apparatus for Three-Dimensional Objects,” US Patent 5,340,433 A (1994).
24. J.E. Smay, G.M. Gratson, R.F. Shepherd, J. Cesarano III, J.A. Lewis, *Adv. Mater.* **14**, 1279 (2002).
25. Q. Li, J.A. Lewis, *Adv. Mater.* **15**, 1639 (2003).
26. D. Therriault, S.R. White, J.A. Lewis, *Nat. Mater.* **2**, 265 (2003).
27. B.A. Tuttle, J.E. Smay, J. Cesarano III, J.A. Voigt, T.W. Scofield, W.R. Olson, J.A. Lewis, *J. Am. Ceram. Soc.* **84**, 872 (2001).
28. J.E. Smay, J. Cesarano III, B.A. Tuttle, J.A. Lewis, *J. Am. Ceram. Soc.* **87**, 293 (2004).
29. K. Sun, T.-S. Wei, B.Y. Ahn, J.Y. Seo, S.J. Dillon, J.A. Lewis, *Adv. Mater.* **25**, 4539 (2013).
30. N.A. Bakhtina, U. Loeffelmann, N. MacKinnon, J.G. Korvink, *Adv. Funct. Mater.* **25**, 1683 (2015).
31. B.H. Cumpston, S.P. Ananthavel, S. Barlow, D.L. Dyer, J.E. Ehrlich, L.L. Erskine, A.A. Heikal, S.M. Kuebler, I.-Y.S. Lee, D. McCord-Maughon, J. Qin, H. Rockel, M. Rumi, X.-L. Wu, S.R. Marder, J.W. Perry, *Nature* **398**, 51 (1999).
32. C.W. Hull, “Apparatus for Production of Three-Dimensional Objects by Stereolithography,” US Patent 4,575,330 (1986).
33. P.F. Jacobs, *Rapid Prototyping & Manufacturing: Fundamentals of Stereolithography* (Society of Manufacturing Engineers, Dearborn, MI, 1992).
34. C. Hull, M. Feygin, Y. Baron, R. Sanders, E. Sachs, A. Lightman, T. Wohlers, *Rapid Prototyp. J.* **1**, 11 (1995).
35. C. Sun, N. Fang, D.M. Wu, X. Zhang, *Sens. Actuators A Phys.* **121**, 113 (2005).
36. S. Kumar, *JOM* **55**, 43 (2003).
37. P. Heini, A. Rottmair, C. Korner, R.F. Singer, *Adv. Eng. Mater.* **9**, 360 (2007).
38. O.L.A. Harrysson, O. Cansizoglu, D.J. Marcellin-Little, D.R. Cormier, H.A. West II, *Mater. Sci. Eng. C* **28**, 366 (2008).
39. T. Buckmann, N. Stenger, M. Kadic, J. Kaschke, A. Frolich, T. Kennerknecht, C. Eberl, M. Thiel, M. Wegener, *Adv. Mater.* **24**, 2710 (2012).
40. E. Yablonovitch, *Phys. Rev. Lett.* **58**, 2059 (1987).
41. J.D. Joannopoulos, P.R. Villeneuve, S. Fan, *Nature* **386**, 143 (1997).
42. S.Y. Lin, J.G. Fleming, D.L. Hetherington, B.K. Smith, R. Biswas, K.M. Ho, M.M. Sigalas, W. Zubrzycki, S.R. Kurtz, J. Bur, *Nature* **394**, 251 (1998).
43. E. Yablonovitch, *Sci. Am.* **285**, 47 (2001).
44. X. Zheng, H. Lee, T.H. Weisgraber, M. Shusteff, J. DeOtte, E.B. Duoss, J.D. Kuntz, M.M. Biener, Q. Ge, J.A. Jackson, S.O. Kucheyev, N.X. Fang, C.M. Spadaccini, *Science* **344**, 1373 (2014).
45. B.G. Compton, J.A. Lewis, *Adv. Mater.* **26**, 5930 (2014).
46. G.S. Chai, S.B. Yoon, J.-S. Yu, J.-H. Choi, Y.-E. Sung, *J. Phys. Chem. B* **108**, 7074 (2004).
47. A.-H. Lu, J.-J. Nitz, M. Comotti, C. Weidenthaler, K. Schlichte, C.W. Lehmann, O. Terasaki, F. Schuth, *J. Am. Chem. Soc.* **132**, 14152 (2010).
48. J. Moorthy, D.J. Beebe, *Lab Chip* **3**, 62 (2003).
49. P. Li, Y. Zong, Y. Zhang, M. Yang, R. Zhang, S. Li, F. Wei, *Nanoscale* **5**, 3367 (2013).
50. K. Boomsma, D. Poulikakos, F. Zwick, *Mech. Mater.* **35**, 1161 (2003).
51. V. Saranathan, C.O. Osuji, S.G.J. Mochrie, H. Noh, S. Narayanan, A. Sandy, E.R. Dufresne, R.O. Prum, *Proc. Natl. Acad. Sci. U.S.A.* **107**, 11676 (2010).
52. L.J. Gibson, *J. R. Soc. Interface* **9**, 2749 (2012).
53. M.E. Launey, M.J. Buehler, R.O. Ritchie, *Annu. Rev. Mater. Res.* **40**, 25 (2010).
54. A. Miserez, T. Schneberk, C. Sun, F.W. Zok, J.H. Waite, *Science* **319**, 1816 (2008).
55. J.C. Weaver, G.W. Milliron, A. Miserez, K. Evans-Lutterodt, S. Herrera, I. Gallana, W.J. Mershon, B. Swanson, P. Zavattieri, E. DiMasi, D. Kisailus, *Science* **336**, 1275 (2012).
56. U.G.K. Wegst, H. Bai, E. Saiz, A.P. Tomsia, R.O. Ritchie, *Nat. Mater.* **14**, 23 (2015).
57. L. Li, J.C. Weaver, C. Ortiz, *Nat. Commun.* **6**, 6216 (2015).
58. A.M. Greiner, B. Richter, M. Bastmeyer, *Macromol. Biosci.* **12**, 1301 (2012).
59. D. Lin, Q. Nian, B. Deng, S. Jin, Y. Hu, W. Wang, G.J. Cheng, *ACS Nano* **8**, 9710 (2014).



60. L.R. Meza, S. Das, J.R. Greer, *Science* **345**, 1322 (2014).
 61. E.B. Duoss, T.H. Weisgraber, K. Hearon, C. Zhu, W. Small IV, T.R. Metz, J.J. Vericella, H.D. Barth, J.D. Kuntz, R.S. Maxwell, C.M. Spadaccini, T.S. Wilson, *Adv. Funct. Mater.* **24**, 4905 (2014).
 62. P. Zhang, J. Toman, Y. Yu, E. Biyikli, M. Kirca, M. Chmielus, A.C. To, *J. Manuf. Sci. Eng.* **137**, 021004 (2015).
 63. L.J. Gibson, M.F. Ashby, *Cellular Solids: Structure and Properties* (Cambridge University Press, Cambridge, UK, 1997).
 64. D. Guo, G. Xie, J. Luo, *J. Phys. D Appl. Phys.* **47**, 013001 (2014).
 65. K. Bian, W. Bassett, Z. Wang, T. Hanrath, *J. Phys. Chem. Lett.* **5**, 3688 (2014).
 66. R. Lakes, *Science* **235**, 1038 (1987).
 67. D. Prall, R.S. Lakes, *Int. J. Mech. Sci.* **39**, 305 (1996).
 68. L. Wang, J. Lau, E.L. Thomas, M.C. Boyce, *Adv. Mater.* **23**, 1524 (2011).
 69. L.S. Dimas, G.H. Bratzel, I. Eylon, M.J. Buehler, *Adv. Funct. Mater.* **23**, 4629 (2013).
 70. L.S. Dimas, M.J. Buehler, *Soft Matter* **10**, 4436 (2014).
 71. M. Gutttag, M.C. Boyce, *Adv. Funct. Mater.* **25**, 3641 (2015).
 72. S.-Z. Guo, X. Yang, M.-C. Heuzey, D. Therriault, *Nanoscale* **7**, 6451 (2015).
 73. H. Gao, B. Ji, I.L. Jager, E. Arzt, P. Fratzl, *Proc. Natl. Acad. Sci. U.S.A.* **100**, 5597 (2003).
 74. K. Jain, M. Klosner, M. Zemel, S. Raghunandan, *Proc. IEEE* **93**, 1500 (2005).
 75. H. Siringhaus, T. Kawase, R.H. Friend, T. Shimoda, M. Inbasekaran, W. Wu, E.P. Woo, *Science* **290**, 2123 (2000).
 76. R.D. Piner, J. Zhu, F. Xu, S. Hong, C.A. Mirkin, *Science* **283**, 661 (1999).
 77. J.J. Adams, E.B. Duoss, T.F. Malkowski, M.J. Motala, B.Y. Ahn, R.G. Nuzzo, J.T. Bernhard, J.A. Lewis, *Adv. Mater.* **23**, 1335 (2011).
 78. J. Hu, M.-F. Yu, *Science* **329**, 313 (2010).
 79. R.C. Chiechi, E.A. Weiss, M.D. Dickey, G.M. Whitesides, *Agnew. Chem. Int. Ed.* **47**, 142 (2008).
 80. M.D. Dickey, R.C. Chiechi, R.J. Larsen, E.A. Weiss, D.A. Weitz, G.M. Whitesides, *Adv. Funct. Mater.* **18**, 1097 (2008).
 81. C. Ladd, J.-H. So, J. Muth, M.D. Dickey, *Adv. Mater.* **25**, 5081 (2013).
 82. M.R. Khan, C. Trlica, M.D. Dickey, *Adv. Funct. Mater.* **25**, 671 (2015).
 83. Y.L. Kong, I.A. Tamargo, H. Kim, B.N. Johnson, M.K. Gupta, T.-W. Koh, H.-A. Chin, D.A. Steingart, B.P. Rand, M.C. McAlpine, *Nano Lett.* **14**, 7017 (2014).
 84. K. Zaghbi, M. Armand, M. Gauthier, *J. Electrochem. Soc.* **145**, 3135 (1998).
 85. X. Zhang, W. Shyy, A.M. Sastry, *J. Electrochem. Soc.* **154**, A910 (2007).
 86. J.A. Lewis, B.Y. Ahn, *Nature* **518**, 42 (2015). □



SAVE THE DATE!

Tuesday
December 1, 2015
#GIVINGTUESDAY™

Support the Materials Research Society Foundation at the 2015 MRS Fall Meeting & Exhibit or online at www.mrs.org/giving-tuesday.

MATERIALS RESEARCH SOCIETY FOUNDATION

INTERNATIONAL CENTRE FOR DIFFRACTION DATA

MAKE THE

SMART

MOVE TO

PDF-4+

S	Standardized data
M	More coverage
A	All data sets are evaluated for quality
R	Reviewed, edited and corrected prior to publication
T	Targeted for material identification and characterization

Featuring

365,877 entries


including

251,640 entries


with atomic coordinates



ICDD databases are the only crystallographic databases in the world with quality marks and quality review processes that are ISO certified.

Visit us at MRS Booth #409



INTERNATIONAL CENTRE FOR DIFFRACTION DATA



www.icdd.com | marketing@icdd.com

ICDD, the ICDD logo and PDF are registered in the U.S. Patent and Trademark Office. Powder Diffraction File is a trademark of JCPDS—International Centre for Diffraction Data ©2015 JCPDS—International Centre for Diffraction Data - 10/15